Facet-dependent adsorption of Pb(II) on hematite (001), (116), and (104) surfaces

Ping Chen,[1] Micah P. Prange,[1] Duo Song,[1] Sungsik Lee,[2] Sang Soo Lee,[3] Juejing Liu,[1] Yatong Zhao,[1] Xiang Wang,[1] Mark H. Engelhard,[4] Yadong Zhou,[4] Yifu Feng,[1] Nikita Basilyan,[1] Xiaoxu Li,[1] Carolyn I. Pearce,[5] Zheming Wang,[1] Zihua Zhu,[4] Kevin M. Rosso[1,]*, and Xin Zhang[1,]*

[1] Physical & Computational Science Directorate, Pacific Northwest National Laboratory, Richland, Washington 99354, United State

[2] X-ray Science Division, Argonne National Laboratory, Lemont, Illinois, 60439, United State

[3] Chemical Sciences and Engineering Division, Argonne National Laboratory, Lemont, IL 60439, United States

[4] Environmental Molecular Sciences Laboratory, Pacific Northwest National Laboratory, Richland, Washington 99354, United States

[5] Energy and Environment Directorate, Pacific Northwest National Laboratory, Richland, Washington 99352, United States

ABSTRACT: Hematite's common (001) and (012) facets are frequently used in model studies of lead (Pb) adsorption behavior, but there is a lack of research on the high-energy facets, e.g. (104), present in nature. Also, few studies have attempted to connect the molecular details of facet-specific Pb adsorption to macroscopic uptake behavior. To address these knowledge gaps, we investigated Pb(II) adsorption behaviors on facet-engineered hematite nanoparticles dominated by (001), (104), and (116). Adsorption experiments revealed significant variations in Pb(II) uptake among the three samples, with (001) demonstrating the highest capacity and (116) showing the best adsorption efficiency when normalized to specific surface area. Adsorption kinetics followed

the pseudo-second-order model, indicating the adsorption process is governed mostly by chemisorption. Adsorption isotherms were well fitted by the Langmuir model, indicating uptake proceeds until roughly monolayer adsorption. Detailed characterization revealed Pb(II) was adsorbed as single atoms with complex inner-sphere binding modes that varied across different facets, indicating adsorption is both structurally and energetically facet-dependent. Co-adsorption experiments further demonstrated Cu^{2+}, Zn^{2+}, and humic acid significantly promoted Pb(II) adsorption. This study advances the understanding of hematite surface reactivity in controlling macroscopic wet adsorption behaviors, providing valuable insights into the environmental fate of Pb(II).

KEYWORDS: Hematite, Lead adsorption, Facet-dependence, Contaminant removal

SYNOPSI: The facet-dependent reactivity of hematite in Pb(II) adsorption enhances our understanding of contaminant removal processes in natural environments.

1. INTRODUCTION

Over the past few decades, the large-scale mining of lead (Pb) resources and the use of Pb-containing materials[1-3] has caused hazardous Pb(II) levels to accumulate in many environmental systems. In particular, Pb concentrations in soils and sediments near metal mining sites often exceed 10000 mg/kg.[4] Given its well-known toxicity,[5, 6] understanding processes that control Pb mobility in the environment is important. Under certain conditions, Pb can precipitate as sparingly soluble minerals ($PbCO_3$, $Pb_5(PO_4)_3Cl$)[7, 8] or be coprecipitated into other phases, e.g., iron oxides or (oxy)hydroxides.[9] However, more commonly Pb mobility is controlled by adsorption onto

mineral surfaces, especially those that possess high reactive surface areas such as the Mn or Fe oxides and hydroxides[10-12] and clay minerals,[13-15] or organic matter.[16-18]

Hematite (α-Fe_2O_3), one of the most thermodynamically stable iron oxides, is widely distributed in the environment.[19] It has abundant surface reactive sites, especially when in nanoparticulate form, leading to high adsorption capacities for metal ions.[20, 21] Hence, Pb(II) adsorption on hematite has been extensively studied by both experimental and theoretical methods. Macroscopic batch adsorption experiments on hematite powders show a strong pH-dependence for Pb uptake by hematite.[22] Bargar et al.[23] used X-ray absorption near-edge structure (XANES) and extended x-ray absorption fine structure (EXAFS) spectroscopy to characterize average Pb surface complexes on hematite powders as a function of pH (6-8), sorption density (2-10 μmoles/m^2), and $[Pb]_{eq}$ (0.2 μM - 1.2 mM) in sodium nitrate ($NaNO_3$, 0.1 M) electrolyte, finding mononuclear bidentate complexes to edges of FeO_6 octahedra with a Pb-Fe distance of 3.3 Å. Lenhart et al.[24] confirmed this edge-sharing structure and found an additional binuclear bidentate corner sharing complex with Pb-Fe distances up to 3.8 Å. Subsequent work focused on Pb complexation on well-defined low-index hematite surface, in part to remove the ambiguities of site averaging and in part because natural hematite particles can display different morphologies varying from platy, prismatic, to spherical shapes.[25, 26] For example, using grazing incidence X-ray absorption fine structure (GI-XAFS) spectroscopy, Bargar et al.[27] found oligomeric Pb(II) complexes binding in inner-sphere modes to both hematite (001) and (012) surfaces. Density functional theory (DFT) calculations confirmed these binding geometries on the hematite (001) surface though Pb-O distances were slightly shorter than those from EXAFS measurements.[28] Noerpel et al.[29] used two different synchrotron-based X-ray techniques (EXAFS, and resonant anomalous X-ray reflectivity, RAXR) to elucidate the coordination environment of Pb on hematite (001), (012), (110) surfaces,

where they found the presence of both inner-sphere and outer-sphere adsorption modes. Crystallographic details were further resolved using 3D X-ray crystal truncation rod (CTR) measurements by Qiu et al.,[30] who found two types of Pb surface complexes on a chemically mechanically polished hematite (012) surface with 3.19 Å and 3.59 Å Pb-Fe distances, respectively. After that, Qiu et al.[31] also found a similar Pb surface complex forming a trigonal pyramid geometry with a Pb-Fe distance of 3.39 Å on an annealed hematite (012) surface. And these studies on adsorption geometries have facilitated the optimization and refinement of surface complexation models.[32, 33] Although these nearly perfect single-facet studies have been informative, Liang et al.[22] demonstrated that Al-doped hematite surfaces, which typically exhibit a higher density of Fe vacancies, show significantly enhanced Pb(II) adsorption capacity, it is important to note that the presence of Fe vacancies alone can have a detrimental effect on the immobilization of Pb(II) cations on pristine hematite.[34]

An unresolved aspect of this body of work is the relative Pb(II) uptake capacity of the various low-index surfaces of hematite, which would enable linking uptake behavior to particle morphology to improve environmental transport models and inform the design of hematite nanoparticles for Pb remediation. For example, Mei et al.[35] studied $U(VI)O_2^{2+}$ adsorption on two hematite facets (001) and (012), and their results indicated UO_2^{2+} adsorption extent on (012) was larger than (001) because of the existence of singly and triply coordinated sites with higher reactivity on (012) while only doubly coordinated sites exist on the (001). A similar phenomenon was also observed for the adsorption of aromatic organoarsenicals on hematite (001) and (012) due to the configuration difference.[36] RAXR study by Noerpel et al's.[29] indicated that Pb adsorption on different hematite facets followed the order of (012) > (110) > (001) at pH 6, and

(110) > (012) > (001) at pH 4 but no attempt was made to test how these relative affinities manifest at the macroscopic batch adsorption scale.

Recent years have seen major advances in size and facet-controlled hematite nanoparticle synthesis, including particles dominated by (001),[29, 37-39] (012),[29, 38, 40] (104),[39, 41] (110),[29, 42, 43] (113),[38, 39] and (116)[44, 45] surfaces. While the (001) facet is thermodynamically the most stable,[46] high-energy facets such as (110), (104), (113) are also commonly present on hematite particles found in nature.[47-49] Such particles provide an opportunity to study facet-specific Pb(II) surface complexation using the molecular precision of X-ray and DFT techniques as well as studying their impacts at the scale of macroscopic batch uptake experiments.

Here we report a first study designed to bridge these molecular to macroscopic scales for Pb(II) adsorption on hematite. Three synthetic hematite particles with predominantly exposed (001), (104), and (116) facets were used as Pb(II) sorbents. Among them, (001) serves as a reference for comparison with literature data, while the higher-energy (104) and (116) facets have not yet been reported for Pb(II) adsorption studies. We measured the pH-dependent macroscopic adsorption isotherms and kinetics, whereas the molecular details of adsorption were characterized by a combination X-ray photoelectron spectroscopy (XPS), time-of-flight secondary ion mass spectrometry (ToF-SIMS), scanning transmission electron microscopy (STEM), EXAFS measurements and DFT calculations. The findings help advance a more comprehensive understanding of factors controlling Pb(II) uptake on hematite surfaces.

2. EXPERIMENTAL METHODS

2.1 Preparation of hematite nanoparticles. Facet-dependent hematite nanoparticles were synthesized following methods used in previous studies.[40, 44, 45] Briefly, a 0.1 M $FeCl_3$ solution was

prepared by dissolving $FeCl_3 \cdot 6H_2O$ (≥ 97%, Sigma-Aldrich) into a mixture of ethanol (Decon Laboratories Ethanol 200 PROOF) and deionized water (18.2 MΩ·cm) ($V_{ethanol}/V_{water}$ = 98:2) under magnetic stirring to form a homogeneous solution at room temperature. Then $CH_3COONa \cdot 3H_2O$ ($NaAc \cdot 3H_2O$, Amresco, pure) was added into the solution (1 M based on the initial volume) and stirred around 1 h at room temperature. 10 mL solution was transferred into a 20 mL Teflon liner, which was sealed into a Parr vessel and then heated at 180°C in an electric oven for 12 h. The products were hexagonal nanoplates predominantly exposing (001) facets. Separately, a 0.025 M $FeCl_3$ solution was prepared by dissolving $FeCl_3 \cdot 6H_2O$ salt into deionized water. 10 mL of this solution was transferred into a 20 mL Teflon liner, which was sealed into a Parr vessel and then heated at 120°C in an electric oven for 3 days, resulting rhombohedral hematite nanocrystals mainly exposing (104) facets. In the third synthesis, 0.001 M $FeCl_3 \cdot 6H_2O$ solution was prepared with deionized water, and 10 mL of the solution was transferred into a 20 mL Teflon liner, which was sealed into a Parr vessel and then heated at 120°C in an electric rotating oven for 2 days. The products were hexagonal bipyramid hematite nanocrystals primarily exposing (116) facets. All the precipitates were recovered by centrifugation and then washed several times with deionized water. The washed solid pastes were then dried in air at 80°C overnight.

2.2 Batch adsorption experiments. Batch Pb(II) adsorption experiments were performed in 15 mL centrifuge tubes under continuous agitation at room temperature. In the first series of experiments, $Pb(NO_3)_2$ (≥ 99.0%, Sigma-Aldrich) was dissolved to 100 mg/L with a pH range of 2-7 to avoid the formation of Pb clusters,[23] and then 5 mg hematite was added into the 5 mL solution to investigate the effect of pH on Pb(II) adsorption. In the second series of experiments, 1 g/L hematite was added into Pb(II) solutions with varying Pb(II) concentrations (10-250 mg/L) at pH 6 to measure the adsorption isotherm. Time-dependent experiments were measured with

specific time intervals by adding 5 mg hematite into 5 mL Pb(II) (100 mg/L) solution. After the adsorption, the suspension was centrifuged and the supernatant samples were analyzed by inductively coupled plasma-optical emission spectrometry (ICP-OES, more details, **see Text S1**, **support information (SI)**) for the residual Pb(II) concentration. The Pb(II) adsorbed solids were washed with deionized water one time, and dried at 80^{o}C overnight for further analysis. All the experiments were performed in a glovebox purged with N_2 gas, and the deionized water used for adsorption was degassed in advance by purging pure N_2 gas (99.999% purity) for a minimum of 60 minutes to avoid CO_2 contamination in the Pb solution.[23, 29, 31] Degassed 0.1 M NaOH and HNO_3 solutions were used for pH adjustment by using Thermo Scientific (110P-01A, America). Given that wastewater contaminated with Pb(II) typically contains a variety of coexisting cations and organic acids, for example, industrial wastewater from electroplating, metallurgy, battery manufacturing, and mining,[50-53] understanding their influence on Pb(II) adsorption is crucial for the of fate Pb(II) in the nature environment. Hence, details of the co-adsorption experiments involving Na^{+}, Mg^{2+}, Ca^{2+}, Cu^{2+}, Zn^{2+}, and humic acid are provided in **Text S2, SI**.

2.3 Solids characterization. X-ray diffraction (XRD) patterns were recorded on a Philips X'pert Multi-Purpose Diffractometer (MPD) (PANAlytical, Almelo, The Netherlands) equipped with a fixed Cu anode operating at 50 kV and 40 mA (2θ range from 5° to 100°). Scanning electron microscopy (SEM) images were collected on a Helios NanoLab 600i SEM instrument (FEI, Hillsboro, OR). A carbon coater was used to coat 5 nm carbon thin films on all samples prior to analysis to improve the imaging quality. High-angle annular dark-field scanning transmission electron microscopy (HAADF-STEM) imaging was performed with an aberration corrected Thermo-Fisher Themis Z scanning/transmission electron microscope (S/TEM) operated at 300 kV. The probe convergence angle and the inner detection angle for HAADF detector were 25 mrad

and 52 mrad, respectively. The sample suspensions were dusted on the holey carbon-coated copper grids (Lacey Carbon, 300 mesh; Ted Pella, Inc.) for STEM observations. XPS measurements were performed with a Physical Electronics Quantera Hybrid Scanning X-ray Microprobe. This system uses a focused monochromatic Al Kα X-ray (1486.7 eV) source for excitation and a spherical section analyzer. The instrument has a 32-element multichannel detection system. The X-ray beam is incident normal to the sample and the photoelectron detector is at 45° off-normal. High energy resolution spectra were collected using a pass-energy of 69.0 eV with a step size of 0.125 eV. For the Ag $3d_{5/2}$ line, these conditions produced a FWHM of 0.92 eV ± 0.05 eV. The binding energy (BE) scale is calibrated using the Cu $2p_{3/2}$ feature at 932.62 ± 0.05 eV and Au $4f_{7/2}$ at 83.96 ± 0.05 eV. ToF-SIMS measurements were conducted using a TOF-SIMS5 instrument (IONTOF GmbH, Münster, Germany). A 25 keV pulsed Bi_3^+ beam served as the analysis beam for collecting SIMS spectra. The Bi_3^+ beam was focused to a diameter of approximately 5 μm and scanned over an area of 200 × 200 μm². The pulsed Bi_3^+ beam (10 kHz) had a current of around 0.56 pA, and data collection took approximately 96 seconds per spectrum. The mass resolution ranged from 5000 to 7000, depending on sample roughness. Charge compensation during measurements was achieved using a low-energy (10 eV) electron flood gun. ToF-SIMS sample preparation involved dispersing the as-prepared samples in water using a sonicator for 5 minutes. The dispersed suspension was then dropped onto a silicon wafer, which was allowed to dry under ambient conditions before being introduced into the chamber. XAFS spectra of Pb L3-edge were collected from hematite samples with (116), (104), and (001) facets treated by 150 mg/L Pb(II) solution in fluorescence mode at beamline 12-BM at Advanced Photon Source, Argonne National Laboratory. A Si(111) monochromator was used to tune the energy of X-ray. We calibrated the energy of the data by using an Pb foil. A 7-element fluorescence detector (Vortex ME7) was used to collect XAFS

spectra of samples in room temperature. The collected data was preprocessed by Athena software with energy calibration, glitch removal, background removal, etc. (see **Table S1, SI** for detailed preprocessing parameters and **Figure S1a** to **c** for processed data in E space).[54] Due to the relatively low concentration of Pb on the hematite, the data in the high K range is noisy. We observed the XAFS wavelet diagram by Xraylarch software (see **Figure S1 d** to **f, SI**) to determine the maximum allowable K range for fitting without including any noise in the high K region, e.g., beyond 9.50 $Å^{-1}$ (see **Figure S1 g** to **I, SI**).[55] After the selection of proper K range, the data was then converted from K3 space into radius distribution function by Fourier transform. The relatively large K range from about 2.50 $Å^{-1}$ to 9.50 $Å^{-1}$ is sufficient to fit the detailed local environment of Pb. Artemis software was used to fit the XAFS data.[54] The potential Pb local environments on (116), (104), and (001) facet were simulated and optimized by DFT simulation. The theoretical scattering patterns were then obtained from DFT-simulated local environment the by *feff6* code.[56] All three fittings exhibited a r^2 smaller than 0.01 (see **Table S1, SI**) indicating that good fittings were reached.[57]

2.4 DFT calculations. All DFT calculations were conducted using the pseudopotential plane-wave DFT approach implemented in the NWPW module of the NWChem computational chemistry package.[58, 59] The Perdue-Burke-Ernzerhof exchange-correlation functional (PBE96) was utilized throughout the PSPW optimization procedure.[60] The DFT + U approach was applied to account for the electron correlation in the localized Fe 3d orbitals.[61] Based on previous studies on goethite,[62] the effective on-site Coulomb and exchange interaction parameters for each Fe atom were set to 4 eV and 1 eV, respectively. Default pseudopotentials contained in NWChem were used. All the pseudopotentials were modified to the separable form suggested by Kleinman and Bylander.[63] Unrestricted calculations were performed because this is a spin-ordered system. To

define the antiferromagnetic structure of hematite, spin penalty functions were used.[62, 64] The Grimme DFT-D3 method for long-range dispersion forces was also used in the calculations.[65] Periodic boundary conditions were used and wavefunction solutions were obtained at the Γ-point with a wavefunction cutoff energy of 100 Ry and a density cutoff energy of 200 Ry. All atomic positions were entirely relaxed in a fixed unit cell using the default NWChem DRIVER optimizer until the forces on the atoms were converged to 10^{-2} eV/Å and the total energy was converged to 10^{-5} eV.

The simulations were carried out by using the hexagonal hematite unit cell (a = b = 5.090 Å, c = 13.892 Å, α = β = 90.0°, γ = 120.0°). We assume all surfaces are hydroxylated O-terminations as typified by contact with aqueous solution.[44] The three surface slabs were taken from previous methods.[44] Briefly, the (001) surface slab was created by expanding the conventional unit cell doubly along a and b directions, resulting in a (2×2) surface slab (a = b = 10.180 Å) with 8 Fe layers. To create the (104) surface, Euler transformation was used to get a new unit cell (a = 9.050 Å, b = 5.090 Å, c = 5.492 Å, α = 90.0°, β = 94.9°, γ = 124.2°) and expanded the cell in a and b directions to obtain a (1×2) slab (a = 9.050 Å, b = 10.180 Å) with 8 Fe layers. The (116) surface was created by expanding the new unit cell (a = 7.483 Å, b = 9.050 Å, c = 10.986 Å, α = 110.2°, β = 95.8°, γ = 63.6°) along a, b direction. We use a (1×1) surface slab consisting of 12 Fe layers. All the slabs consist of an upper and a lower surface with the same outmost atomic layer and a vacuum of approximately 10 Å in between. Both (001) and (104) surface slabs consisted of 32 Fe, 60 O and 24 H atoms while (116) slab had 24 Fe, 46 O and 20 H atoms and with the thickness of slab 9.6 Å, 13.9 Å and 11.3 Å, respectively, which corresponds to the distance in c direction between two oxygen atoms on surface. The three surfaces were modeled by fully relaxed slabs without inversion symmetry. Initial adsorbed Pb(II) positions prior to energy minimization were

selected on a chemically intuitive basis informed by adsorbed geometries determined in prior studies. Water molecules completing the solvation spheres of the adsorbed Pb(II) cations were not added due to the soft acid character of the Pb(II) cation and to avoid the attendant computational expense of configuration sampling. Adsorbed Pb(II) energy minimizations were performed letting all atoms in the slab relax. Finally, the standard energy difference method[44] was applied to calculate the adsorption energy (E_{ads}) per unit surface area, give as:

$$E_{ads} = (E_{Hem+Pb(II)} - E_{Hem} - E_{Pb(II)})/A$$

Where $E_{Hem+Pb(II)}$ represents the total energy of the optimized Pb(II) adsorbed complex on the hematite surface, E_{Hem} is the energy of the corresponding hematite surface, $E_{Pb(II)}$ is the energy of a free Pb(II) ion in vacuum, and A is the area of the slab surface.

3. RESULTS AND DISCUSSION

3.1 Characterization of hematite nanoparticles. The morphological characteristics of the synthesized hematite nanoparticles (**Figure 1**) were consistent with those reported in previous works.[40, 44, 45] **Figure 1a** illustrates hexagonal hematite nanoplatelets characterized by two prominent (001) basal facets and twelve (012) edge facets with particle sizes at 250 – 300 nm. The surface area ratio between the (001) and (012) facets is approximately 9:1 according to previous report.[40] **Figure 1b** shows a rhombic morphology with six (104) facets, and particle sizes around 50 nm. **Figure 1c** shows a hexagonal bipyramidal morphology with twelve (116) facets, and particle sizes of 200 - 300 nm. The XRD patterns (**Figure 1d**) confirmed that all samples were pure hematite (JCPDS No. 33-0664) with high crystallinity showing (012), (104), (110), (113), (204), (116), (018), (214) and (030) lattice planes, respectively.

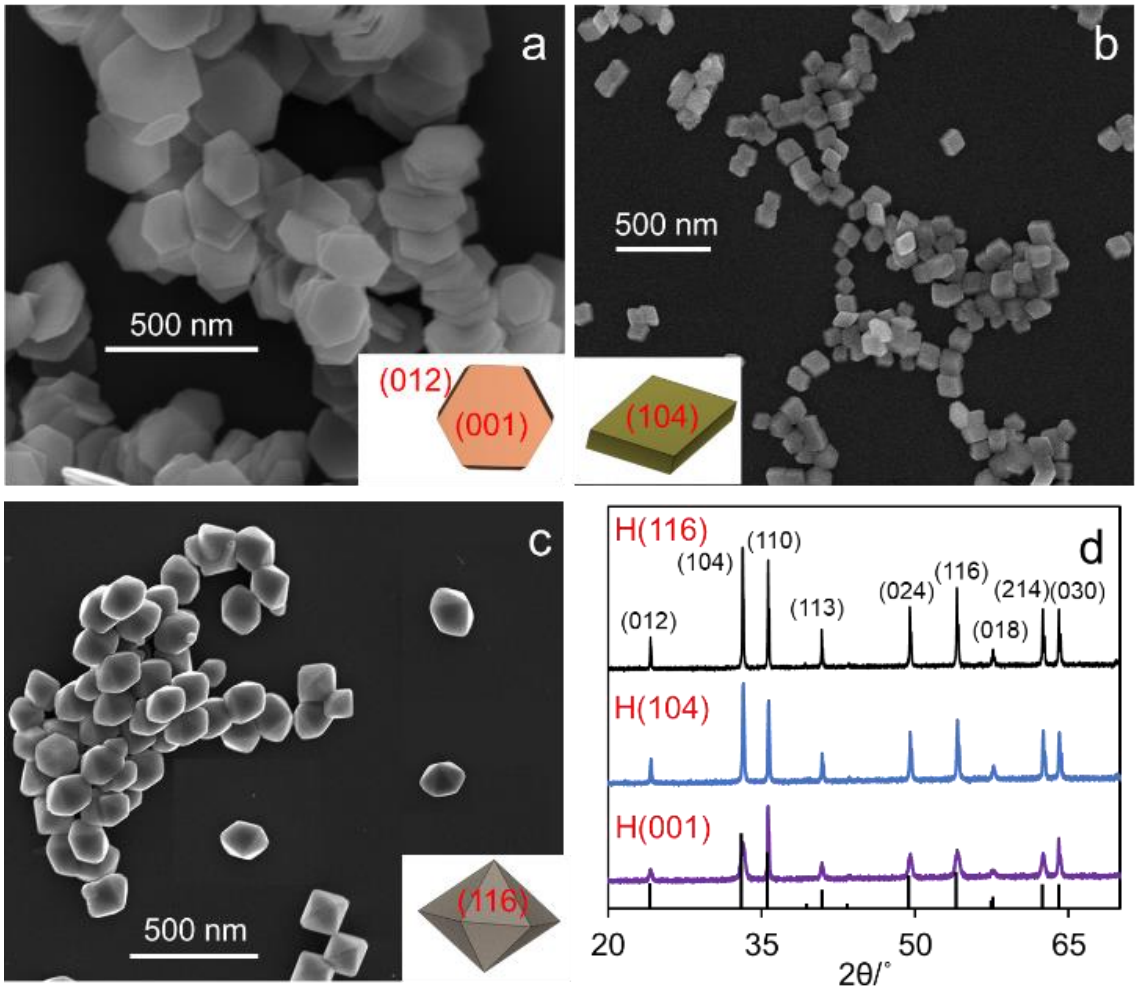

Figure 1. STEM images (a, b, c) and XRD patterns (d, with inserted JCPDS No. 33-0664) of the three different hematite particle types used in this study.

3.2 Adsorption of Pb(II). Pb(II) adsorption was examined on different hematite facets under varying pH, reaction time, and aqueous Pb(II) concentration. We find that the total Pb(II) uptake (**Figure 2a, c, e**) was in the order (001) > (104) > (116), where the highest Pb(II) adsorption capacity for (001) is consistent with its largest specific surface area. However, when normalized by surface area (**Figure 2b, d, f**) the (116) particles show the highest Pb(II) adsorption efficiency. In particular, Pb(II) loading amounts below pH 5.0 did not change much for different hematite particles but gradually increased when the pH was higher than 5.0. This is expected based on the

pH_{ZPC} of hematite at 7~9,[66, 67] below which the surface carries a net positive charge and electrostatically repels Pb(II). In kinetic studies, we found that Pb(II) adsorption equilibrium was usually reached in less than 100 minutes. We applied the pseudo-first- and pseudo-second-order kinetic models[68] to fit the data (**Figure S2, Table S2, SI**). The pseudo-second-order model generally provided a better fit ($R^2 > 0.97$) with a q_e (equilibrium adsorption efficiency) of 0.49, 0.52, and 1.71 mg/m^2 for (001), (104), and (116), respectively. The adsorption rates for (001), (104), and (116) were 0.09, 0.13, and 0.04 $m^2mg^{-1}min^{-1}$, respectively. The results show that while (104) particles exhibit the fastest adsorption rate, (116) particles have a higher adsorption efficiency. The best fit to the kinetic data indicates that Pb(II) uptake is likely by chemisorption.[69] In the adsorption isotherm studies, we found both Langmuir and Freundlich isotherm models[70, 71] fit well, but the Langmuir model gave a better fit (**Figure S3, Table S3, SI**) with a q_{max} (saturated adsorption efficiency) of 1.06, 1.79, and 9.52 mg/m^2 for (001), (104), and (116), respectively. These results indicate that Pb(II) likely sorbs onto hematite as a monolayer.[72] Compared to the maximum Pb adsorption capacities of naturally occurring materials (**Table 1**), particularly spherical (irregular) hematite and outperforming hematite (012), the hematite crystal facets investigated in this study exhibit significantly higher adsorption levels.[73, 74] Since naturally occurring hematite typically appears in irregular forms or predominantly exposes facets like (001) and (104),[47, 49] these findings highlight the critical role of crystal facet engineering in influencing Pb(II) mobility and transformation in natural environments. By selectively exposing or optimizing high-performance facets, the adsorption capacity for Pb(II) can be markedly enhanced, demonstrating the potential of tailored crystal properties to advance hematite's effectiveness in environmental remediation applications.

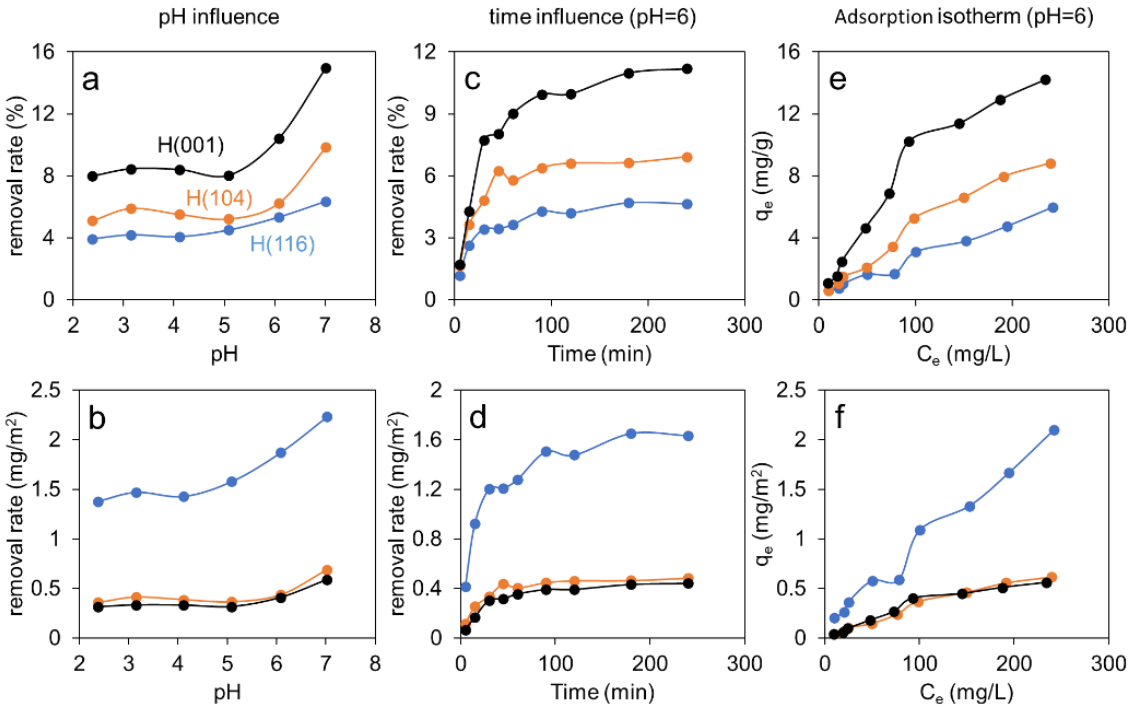

281

282 **Figure 2.** Pb(II) adsorption onto the three different hematite nanoparticles in terms of (a, b) pH
283 influence, (c, d) adsorption kinetics, and (e, f) adsorption isotherms. b, d, and f were normalized
284 by BET surface area using a, b, c, respectively.
285

Table 1. Maximum adsorption capacity of Pb(II) onto various adsorbents

Common mineral adsorbents	Conditions	Maximum adsorption capacity (mg/g)
Hydroxyapatite[75]	pH 5, 25 °C	320
Raw kaolinite[76]	Natural pH, 30 °C	4.73
Palygorskite[77]	pH 5, 20 °C	17.39
Goethite and Mn substituted[78]	pH 5, 25 °C	16.34 to 90.09
diatomite[79]	pH 4, 23 °C	24
Nature calcite[80]	pH 7, 25 °C	19.92
Montmorillonite[81]	pH 6.0, 25 °C	57.0
β-MnO_2[82]	pH 5.50, 25 °C	13.57
Hematite (012)[74]	pH 5.50, 25 °C	13.79
Spherical hematite[73]	pH 5.50, 25 °C	15.3
Hematite (001), this study	pH 6, 25 °C	26.26
Hematite (104), this study	pH 6, 25 °C	25.54
Hematite (116), this study	pH 6, 25 °C	21.94

3.3 Pb(II) adsorption mechanisms. After evaluating macroscopic batch Pb(II) loading capacity/efficiency through wet chemical experiments, we then analyzed Pb(II)-adsorbed particle surfaces to determine adsorption geometries. First, XPS data (**Figure 3a, b, c**) confirmed that Pb(II) was successfully adsorbed onto hematite, with the Pb 4f peak present at ~141.63 and ~136.25 eV.[83, 84] The adsorption intensity increased in the following order: (001) ≈ (104) < (116). This is generally consistent with the macroscopic adsorption efficiency results shown in **Figure 2b, d, f**. ToF-SIMS (**Figure 3d, e**) was applied to determine whether Pb(II) was adsorbed as single atoms or clusters (schematic in **Figure S4, SI**). We could identify large amounts of Pb^+ (m/z = 207) and $PbOFe^+$ (m/z = 279) but negligible amounts of $PbOPb^+$ (m/z = 430), leading to the conclusion that Pb adsorbs as single atoms and Pb-O-Pb bonds tend not to be formed on the hematite surface. This conclusion was further supported by atomically resolved STEM imaging.

Figure 4 shows bright spots (indicated by red arrows), consistent with single adsorbed Pb atoms against the high-resolution lattice fringes of background hematite.

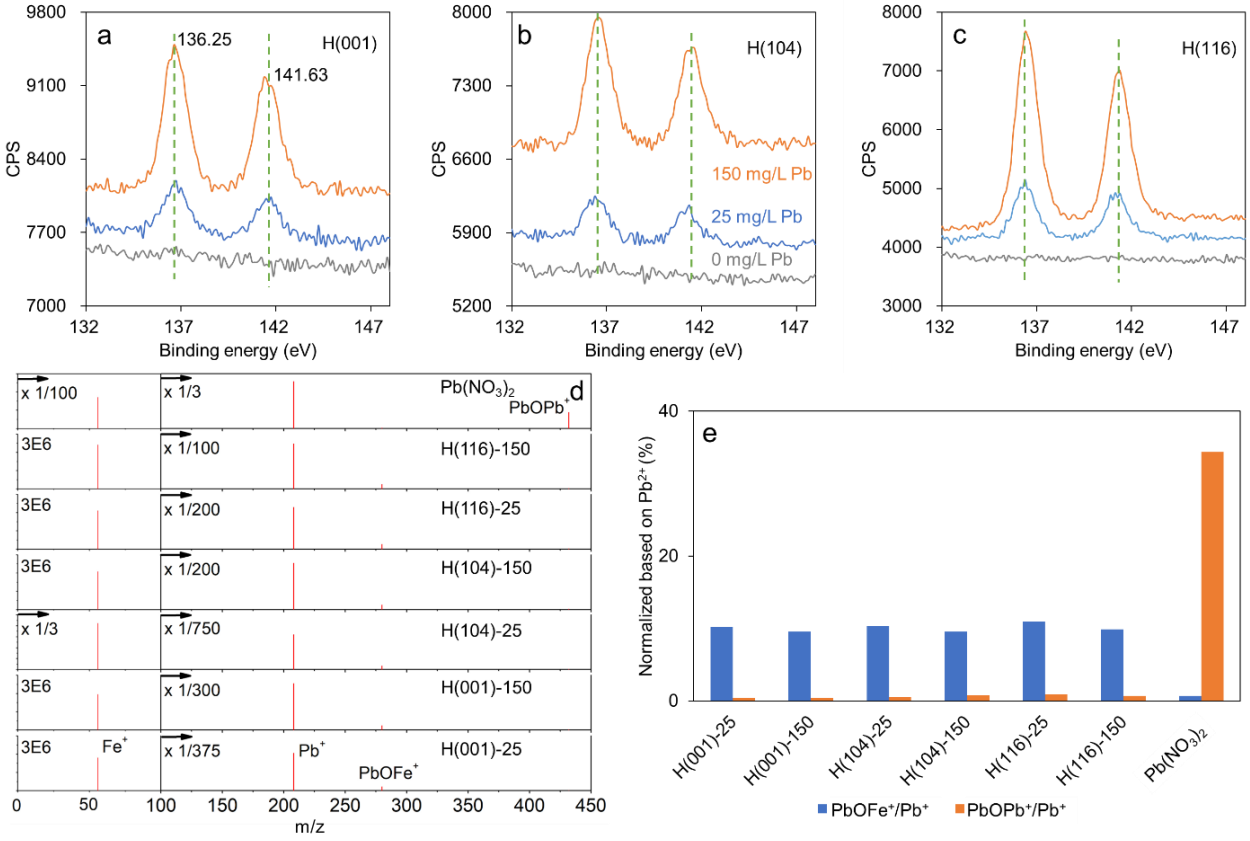

Figure 3. High-resolution XPS results of Pb 4f spectra (a, b, c) for hematite before and after Pb (II) adsorption, ToF-SIMS results (d, positive ion spectra) of hematite after Pb(II) adsorption, and their normalized relative ratio (e).

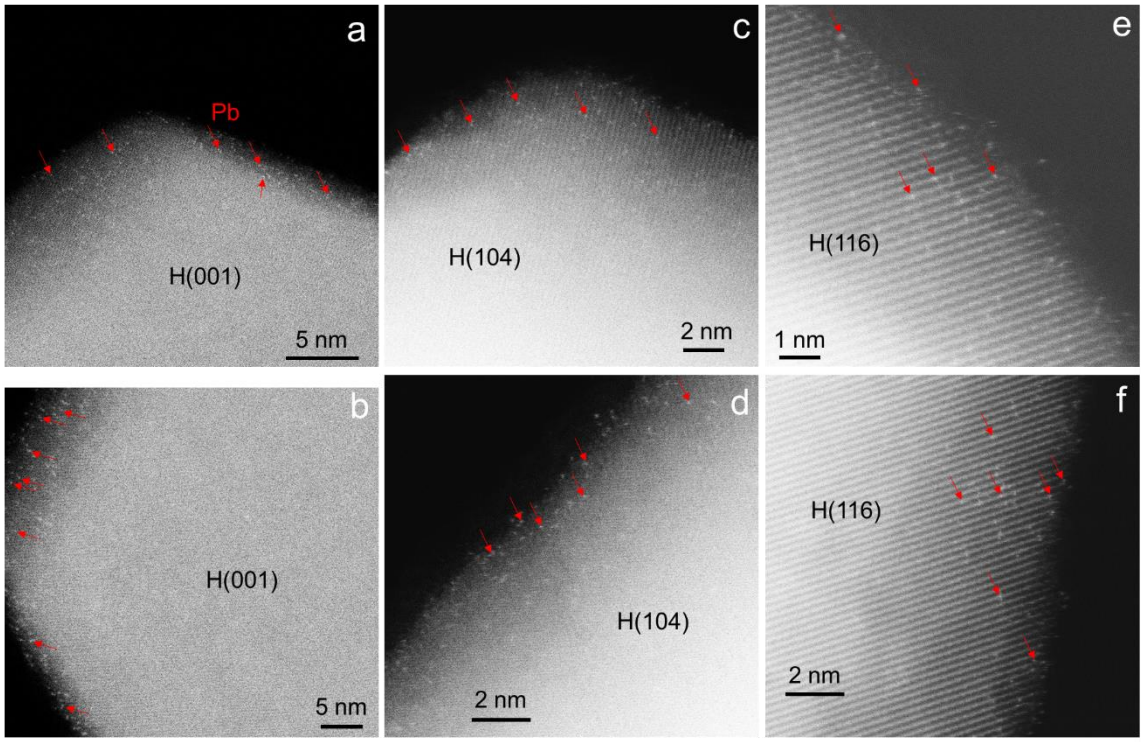

Figure 4. HAADF-STEM images of Pb(II) adsorbed hematite (initial Pb concentration: 150 mg/L). The bright features indicated by red arrows are consistent with individual adsorbed Pb atoms.

In anticipation of the need for molecular structure insights to help interpret our Pb L3 EXAFS measurements, we carried out DFT calculations to search for energetically stable adsorbed Pb(II) structures on the three different hematite surfaces (**Figure 5, Table 2**). For the (001) surface, the calculations indicate that there are three stable tridentate facing-sharing (FS) Pb(II) configurations. In the H(001)-Pb1 configuration (**Figure 5a, Table 2**), the Pb-O distances are uniformly 2.23 Å with a coordination number (CN) of 3.0, and the shortest Pb-Fe distance is 3.01 Å (CN 1.0). In the configuration of H(001)-Pb2 (**Figure 5b, Table 2**), the Pb-O distances are 2.17 Å and 2.44 Å with CN of 2.0 and 1.0, respectively, while the shortest Pb-Fe distance is 3.17 Å (CN 1.0). In the third H(001)-Pb3 configuration (**Figure 5c, Table 2**), the Pb-O distances are 2.19 Å and 2.25 Å with CN of 2.0 and 1.0, respectively, while the shortest Pb-Fe distance is 3.68 Å (CN 1.0). For the (104) surface, three Pb(II) adsorption configurations were identified through the bridging of singly- and

doubly-coordinated oxygen groups. The H(104)-Pb1 (**Figure 5d, Table 2**) presents a tridentate FS arrangement, where Pb(II) is bonded to two singly-coordinated and one doubly-coordinated oxygen groups, with Pb-O lengths of 2.23 and 2.30 Å. The nearest Fe (CN 1.0) is 3.25 Å away from Pb(II). Another configuration of H(104)-Pb2 (**Figure 5e, Table 2**) showing Pb(II) adsorbed as a bidentate corner-sharing (CS) complex to singly- and doubly-coordinated oxygen groups with Pb-O distances of 2.10 and 2.22 Å, respectively, while the closest Fe (CN 2.0) is 3.60 Å away. The third configuration of H(104)-Pb3 (**Figure 5f, Table 2**) also exhibits a tridentate FS complex with Pb(II) bonded to two singly-coordinated and one doubly-coordinated oxygen groups at Pb-O distances of 2.16, 2.29, and 2.66 Å, respectively, and the smallest Pb-Fe distance (CN 1.0) is 3.49 Å. For the (116) facet, two Pb(II) adsorbed geometries of tridentate FS were released showing Pb(II) bound to three singly-coordinated peak-oxygens (H(116)-Pb1, **Figure 5g, Table 2**) or one doubly coordinated valley-oxygen and two singly coordinated peak-oxygens (H(116)-Pb2, **Figure 5h, Table 2**). The Pb-O lengths in H(116)-Pb1 are 2.22 and 2.32 Å (CN 2.0, 1.0, respectively) or 2.22 and 2.26 Å (CN 1.0, 2.0, respectively) in H(116)-Pb2. The shortest Pb-Fe distances are 3.45 Å (CN 2.0) and 3.08 Å (CN 1.0) respectively. Additionally, the negative calculated adsorption energy (E_{ads}) confirmed that Pb(II) adsorption is thermodynamically favorable across the different hematite surfaces. Within each individual surface, our calculations revealed that the variations in E_{ads} among different Pb(II) adsorption configurations were minimal, suggesting no specific preferential adsorption sites for Pb(II) on that surface. In contrast, significant differences in adsorption energy were observed between crystal facets, indicating a clear surface preference for Pb(II) adsorption. Specifically, Pb(II) adsorption on (001) is energetically most favorable, followed by (116), and then (104), consistent with the experimental results, demonstrating Pb(II) adsorption is not only structurally but also energetically facet-dependent.

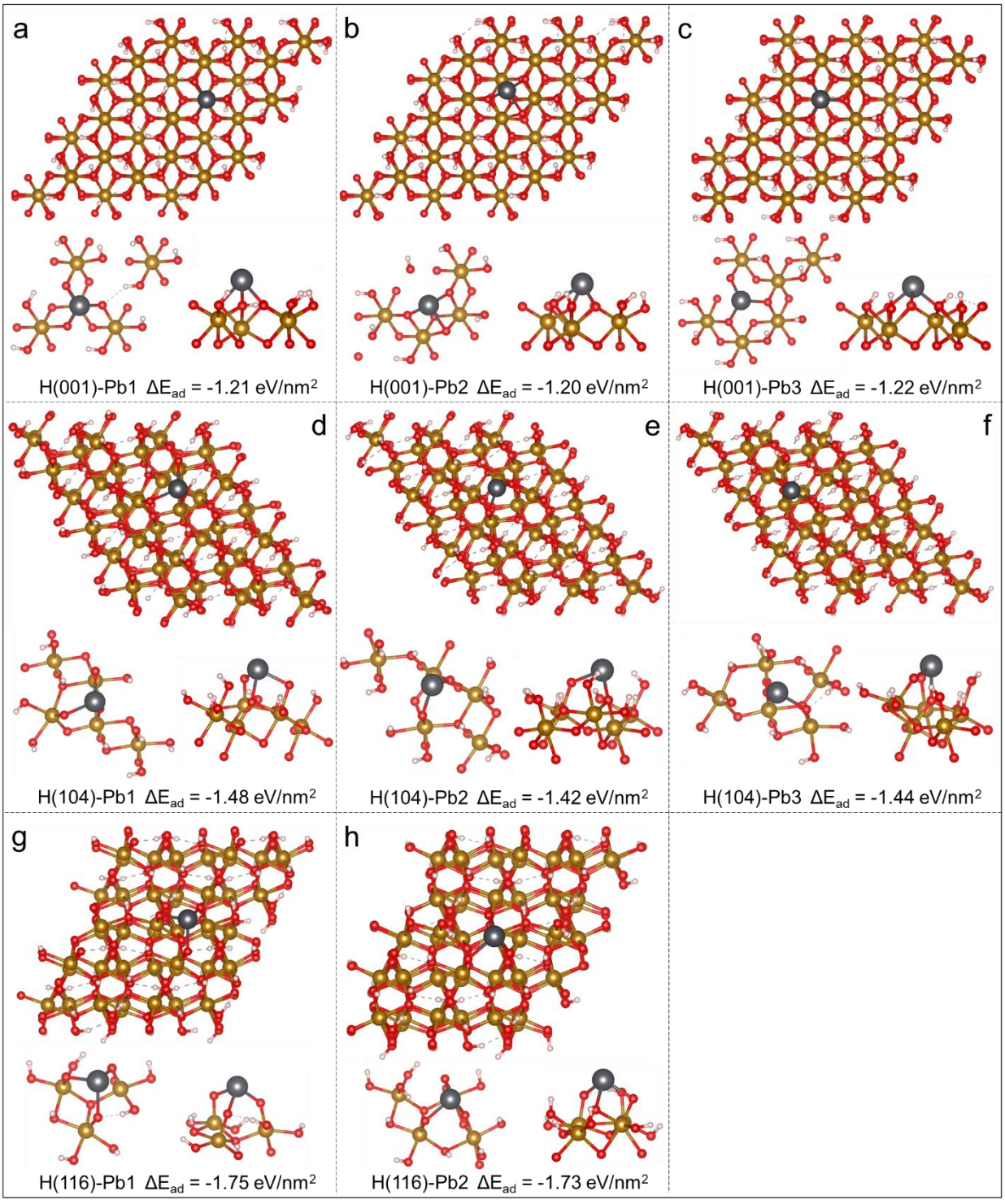

Figure 5. The calculated Pb(II) adsorption complexes on different hematite surfaces from DFT (top view; inserted left: magnified top view; inserted right: side view along [010] direction. The red, white, brown and grey balls correspond to oxygen, hydrogen, iron and lead atoms respectively.).

Table 2. Calculated Pb(II) adsorption complexes on different hematite surfaces from **Figure 5**

Pb(II) geometries	Path	CN	R(Å)	Pb(II) geometries	Path	CN	R(Å)
H(001)-Pb1	Pb-O	3	2.23	H(116)-Pb1	Pb-O1	2	2.22
	Pb-Fe	1	3.01		Pb-O2	1	2.32
H(001)-Pb2	Pb-O1	2	2.17		Pb-Fe	2	3.45
	Pb-O2	1	2.44	H(116)-Pb2	Pb-O1	1	2.22
	Pb-Fe	1	3.17		Pb-O2	2	2.26
H(001)-Pb3	Pb-O1	2	2.19		Pb-Fe	1	3.08
	Pb-O2	1	2.25	H(104)-Pb1	Pb-O1	2	2.23
	Pb-Fe	2	3.68		Pb-O2	1	2.30
H(104)-Pb3	Pb-O1	1	2.16		Pb-Fe	1	3.25
	Pb-O2	1	2.29	H(104)-Pb2	*Pb-O1*	1	2.10
	Pb-O3	1	2.66		Pb-O2	1	2.22
	Pb-Fe	1	3.50		Pb-Fe	2	3.60

Note: *CN*, coordination number; *R*, modeled bond length.

These DFT-predicted stable Pb(II) configurations were used as model systems for linear combination fits to our measured Pb L3 EXAFS spectra. Our XAFS fitting results (**Figure 6, Table S4**) indicate that the local environment of Pb single atoms on different hematite facets is consistent with DFT simulations. While the Pb-O scattering analysis is complex due to potential interactions between water molecules and the Pb single atoms,[85] the Pb-Fe distances obtained from XAFS fitting closely match the DFT-simulated results. For the (116) facet (**Figure 6a**), we identified five Pb-O scattering paths ranging from 1.86 Å to 3.31 Å. The paths at 2.28 Å and 3.31 Å agree well with the DFT-simulated Pb-O distances H(116)-Pb1 at 2.22 Å and 3.39 Å, respectively. The Pb-Fe scattering path is located at 3.43 Å, which is also close to its simulated counterpart at 3.45 Å. The situation for the (001) facet is more complex due to the presence of two potential Pb adsorption sites (**Figure 6b**). Four Pb-O scattering paths were observed, ranging from 1.84 Å to 3.23 Å, along with one Pb-Fe scattering path at 2.96 Å. The Pb-O scattering at 2.28 Å likely corresponds to one

of the potential Pb locations, with a theoretical Pb-O distance of 2.23 Å. The Pb-Fe scattering path for this site, predicted at 3.92 Å, was not observed, potentially due to the long distance and resulting weak scattering. For the second Pb location on the (001) facet, we observed one Pb-O scattering path at 2.49 Å and one Pb-Fe scattering path at 2.96 Å, in good agreement with their theoretical locations at 2.44 Å and 3.01 Å. Hence, the best corresponding configuration for the Pb L3 EXAFS spectra of the (001) samples was H(001)-Pb1. On the (104) facet (**Figure 6c**), all expected Pb-O and Pb-Fe scattering paths were identified in the XAFS data. Two Pb-O scattering paths were located at 2.38 Å and 2.62 Å, matching well with the theoretical distances of the H(104)-Pb3 configuration at 2.29 Å and 2.63 Å, respectively. The Pb-Fe distance was observed at 3.48 Å, close to its theoretical value of 3.50 Å. Our fittings were consistent with previously reported distances of Pb-O at approximately ~2.3 Å (first-shell) while there are some discrepancies in Pb-Fe distance at approximately 3.3 - 3.9 Å (second-shell).[23, 29, 86]

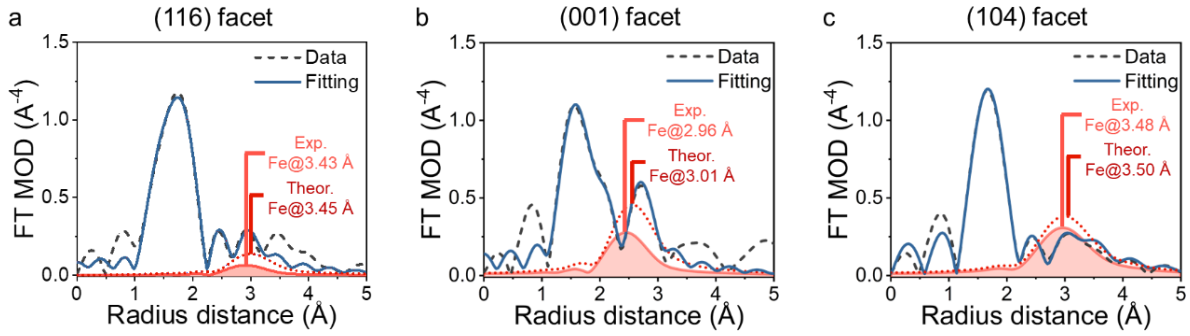

Figure 6. Analysis of Pb local environments on different hematite facets by Pb L3-edge XAFS, including (116) facet (a), (001) facet (b), and (104) facet (c).

3.4 Surface structural information. Based on the above analysis, we constructed representative surface configurations for single Pb(II) atom adsorption on three different hematite facets, each with distinct adsorption complexes. For the (001) particle, the surface oxygen atoms are doubly coordinated to Fe atoms and lie on the same plane (**Table 3, Fig. S5, SI**).[87, 88] Our results show that this arrangement of oxygen atoms is more likely to lead to formation of a tridentate Pb adsorption structure with a Pb-O distance of 2.23 Å, and the Pb-bonded O triply coordinated directly to the single Fe atom. This explains why the Pb-Fe distance in this study is only 3.0 Å. Our Pb complex matches a previous DFT calculation for Pb adsorption on the (001) facet of hematite, which also identified a tridentate configuration with a similar Pb-Fe distance.[28] Although our Pb-Fe distance is much smaller than the other reported Pb-Fe distance,[29] based on the good agreement between the EXAFS data and many of our DFT Pb-Fe distances, our structural results are reasonable. For the (104) particles, this surface consists of equal numbers of singly-, doubly- and triply-coordinated surface oxygen groups, that are arranged from the outermost to the inner layer as singly-, doubly-, and triply-coordinated (**Table 3, Fig. S6, SI**).[39, 44, 87] Among these oxygen groups, singly and doubly coordinated groups are considered active adsorption sites, while triply coordinated groups are inactive and do not participate in adsorption. Thus, the chemical activity follows the order: singly > doubly > triply coordinated groups.[89] Our analysis indicates Pb(II) adsorption happens in a tridentate inner-sphere geometry at the surface, bonding to two singly and one doubly coordinated oxygen groups. The (116) surface is more complicated, with singly, doubly, and triply coordinated surface oxygen groups at a concentration ratio of 2:1:2 (**Table 3, Fig. S7, SI**).[44] These coordinated oxygen atoms are arranged in a series of "ridges" and "valleys" along the *a*-axis direction. This leads to a dense arrangement of singly coordinated

oxygen groups on the top layer. Hence Pb(II) is likely bonding to these singly coordinated oxygen groups forming a tridentate inner-sphere configuration.

Table 3. Hydroxyl density on different hematite facets and Pb(II) saturated adsorption efficiency obtained from theoretical calculations and experimental data

	Singly	Doubly	Triply	Effective adsorption site number*	q_{max} **	BET	q_{max}***
	(site/nm^2)	(site/nm^2)	(site/nm^2)	(10^{18} site/m^2)	(mg/m^2)	(m^2/g)	(mg/m^2)
H(001)	0	13.3	0.0	8.89	18.40	25.35	1.06
H(104)	5.3	5.3	5.3	2.65	5.49	14.26	1.79
H(116)	6.6	3.3	6.6	1.65	3.42	2.85	9.52

Note: * calculated based on the Pb(II) adsorption geometry. ** theoretically calculated based on the effective adsorption site number. *** obtained from the adsorption isotherm fits

Since we now understand the Pb(II) complexation structures on different hematite surfaces and the hydroxyl density (**Table 3**), we can deduce the effective number of adsorption sites, which are 8.89, 2.65, and 1.65 × 10^{18} site/m², for (001), (104), and (116) respectively. Based on these results, we calculated the theoretical Pb(II) saturation adsorption efficiencies, which are 18.40, 5.49, and 3.42 mg/m², showing (001) > (104) > (116). However, this is the opposite of the saturation adsorption efficiencies we obtained from the fitting results of experimental adsorption isotherms. The observed anomaly suggests that on the (001) or (104) surfaces, more hydroxyl groups did not participate in the adsorption reaction. Furthermore, it indirectly implies that the Pb(II) adsorption on the (116) surface is stronger than on the (104) and (001) surfaces, which is highly consistent with the adsorption energy results obtained from our DFT calculations. The likely reason is that on the (116) surface, Pb is coordinated through singly coordinated oxygen groups, while on the (104) surface, Pb(II) is linked by two singly and one doubly coordinated oxygen group, and on the

(001) surface, Pb(II) is connected via three doubly coordinated oxygen groups. On the other hand, the difference in Pb adsorption rates, with (104) > (001) > (116), is likely due to the combined effect of variations in surface potential adsorption sites and the strength of Pb bonding.

3.5. Co-adsorption effects. The results of the co-adsorption experiments are presented in Figure S8 (SI). Compared to the control, Na^{+}, Mg^{2+}, and Ca^{2+} had minimal impact on Pb(II) adsorption across all hematite samples. This limited effect is attributed to their outer-sphere (i.e., physical) adsorption mechanisms, which involve weaker interfacial interactions than the inner-sphere chemical adsorption of Pb(II).[90] In contrast, the presence of Cu^{2+} and Zn^{2+} significantly enhanced Pb(II) adsorption (**Table S5**, SI), with the extent of enhancement depending on the specific hematite facet. This effect is likely due to the inner-sphere adsorption of Cu^{2+} and Zn^{2+},[91, 92] which facilitates the formation of ternary Hem–Cu/Zn–Pb complexes. Notably, the enhancement was more pronounced on the (001) and (104) facets than on the (116) facet, aligning with the respective adsorption capacities of Cu^{2+} and Zn^{2+}, as shown in **Table S5** (SI): (001) > (104) > (116).

HA also significantly increased Pb(II) adsorption, likely due to its abundance of hydroxyl functional groups that promote Pb(II) complexation. Interestingly, the adsorption enhancement was similar regardless of whether HA was introduced before or simultaneously with Pb(II), suggesting that HA initially adsorbs to the hematite surface and then binds Pb(II). The facet-specific adsorption trend remained unchanged—(001) > (104) > (116)—reflecting differences in the density of available adsorption sites.

Overall, these results demonstrate that coexisting species commonly found in industrial wastewater can markedly influence Pb(II) adsorption behavior. They highlight the importance of accounting for complex multi-component interactions in environmental risk assessments and the design of effective heavy metal remediation strategies.

4 ENVIRONMENTAL IMPLICATIONS

This study provides valuable insights into the relationship between atomic-scale hematite surface structures and the macroscopic behavior of Pb(II) adsorption, with important implications for understanding and managing Pb(II) mobility in environmental systems. These findings also hold theoretical significance for improving surface complexation models, such as the CD-MUSIC model, by incorporating facet-specific reactivity as a predictive framework for Pb(II) adsorption at contaminated sites.

Our results demonstrate that the reactivity of different hematite crystal facets influences the adsorption configuration, bonding strength, and overall kinetics and capacity of Pb(II) uptake. These factors collectively govern the sequestration or mobility of Pb(II) in natural environments, including soils, sediments, and groundwater. While the primary focus of this study is on adsorption geometries, we have extended our analysis to include the influence of environmental complexities such as natural organic matter (NOM) and competing cations. By integrating these variables with the facet-specific data, this work enhances the predictive understanding of heavy metal behavior in both natural and engineered settings, contributing to more effective and sustainable contamination management.

Furthermore, the observed facet-dependent adsorption behavior underscores the importance of a nuanced understanding of mineral surface chemistry in environmental applications. This knowledge can guide the design of targeted remediation strategies, including engineered hematite materials or composites that expose highly reactive facets to optimize adsorption performance. These materials may offer improved removal efficiency for Pb(II) and other toxic metals in contaminated waters.

Lastly, our application of ToF-SIMS highlights its value as a powerful tool for characterizing single-atom and cluster adsorption on mineral surfaces. This technique offers a direct method for monitoring trace metal interactions at the atomic scale and holds significant potential for advancing environmental monitoring. By enabling real-time, high-resolution analysis of contaminant behavior in complex systems, ToF-SIMS can play a vital role in assessing and optimizing remediation efforts.

ASSOCIATED CONTENT

Supporting Information

The Supporting Information is available free of charge at …

Additional experimental details in ICP-OES tests and co-adsorption setting; summaries of EXAFS linear combination fitting results; adsorption kinetics and isotherm fitting data; schematic illustration of ToF-SIMS analysis; surface structure models of different hematite facets; co-adsorption experiment results.

AUTHOR INFORMATION

Corresponding Authors

Kevin M. Rosso - *Physical & Computational Science Directorate, Pacific Northwest National Laboratory, Richland, Washington 99354, United States;* https://orcid.org/0000-0002-8474-7720; Email: kevin.rosso@pnnl.gov

Xin Zhang - *Physical & Computational Science Directorate, Pacific Northwest National Laboratory, Richland, Washington 99354, United States;* https://orcid.org/0000-0003-2000-858X; Email: xin.zhang@pnnl.gov

Authors

Ping Chen - *Physical & Computational Science Directorate, Pacific Northwest National Laboratory, Richland, Washington 99354, United States*; https://orcid.org/0000-0002-4527-4561

Micah P. Prange - *Physical & Computational Science Directorate, Pacific Northwest National Laboratory, Richland, Washington 99354, United States*; https://orcid.org/0000-0002-0775-2024

Duo Song - *Physical & Computational Science Directorate, Pacific Northwest National Laboratory, Richland, Washington 99354, United States*; https://orcid.org/0000-0002-5136-7959

Sungsik Lee - X-ray Science Division, Argonne National Laboratory, Lemont, Illinois, 60439, United State; https://orcid.org/0000-0002-1425-9852

Sang Soo Lee - Chemical Sciences and Engineering Division, Argonne National Laboratory, Lemont, IL 60439, United States; https://orcid.org/0000-0001-8585-474X

Juejing Liu - *Physical & Computational Science Directorate, Pacific Northwest National Laboratory, Richland, Washington 99354, United States*; https://orcid.org/0000-0003-4141-8174

Yatong Zhao - *Physical & Computational Science Directorate, Pacific Northwest National Laboratory, Richland, Washington 99354, United States*; https://orcid.org/0000-0002-4659-2924

Xiang Wang - *Physical & Computational Science Directorate, Pacific Northwest National Laboratory, Richland, Washington 99354, United States*; https://orcid.org/0000-0002-9629-3084

Mark H. Engelhard - *Environmental Molecular Sciences Laboratory, Pacific Northwest National Laboratory, Richland, Washington 99354, United States*; https://orcid.org/0000-0002-5543-0812

Yadong Zhou - *Environmental Molecular Sciences Laboratory, Pacific Northwest National Laboratory, Richland, Washington 99354, United States*; https://orcid.org/0000-0002-9012-7536

Yifu Feng - *Physical & Computational Science Directorate, Pacific Northwest National Laboratory, Richland, Washington 99354, United States*;

Nikita Basilyan - *Physical & Computational Science Directorate, Pacific Northwest National Laboratory, Richland, Washington 99354, United States*;

Xiaoxu Li - *Physical & Computational Science Directorate, Pacific Northwest National Laboratory, Richland, Washington 99354, United States*; https://orcid.org/0000-0002-9076-3057

Carolyn I. Pearce - *Energy and Environment Directorate, Pacific Northwest National Laboratory, Richland, Washington 99352, United States*; https://orcid.org/0000-0003-3098-1615

Zheming Wang - *Physical & Computational Science Directorate, Pacific Northwest National Laboratory, Richland, Washington 99354, United States*; https://orcid.org/0000-0002-1986-4357

Zihua Zhu - *Environmental Molecular Sciences Laboratory, Pacific Northwest National Laboratory, Richland, Washington 99354, United States*; https://orcid.org/0000-0001-5770-8462

Notes

The authors declare no competing financial interest.

ACKNOWLEDGEMENTS

This material is based upon work supported by the U.S. Department of Energy (DOE), Office of Science, Office of Basic Energy Sciences, Chemical Sciences, Geosciences, and Biosciences Division through its Geosciences Program at Pacific Northwest National Laboratory (PNNL) (FWP# 56674). PNNL is operated for DOE by Battelle Memorial Institute under Contract DE-AC05-76RL01830. Part of the research was performed with a user proposal #51382 (Award DOI: 10.46936/lser.proj.2020.51382/60000186), 61223 (Award DOI: 10.46936/lsr.proj.2024.61223/60012698) and 51922 (Award DOI: 10.46936/lser.proj.2021.51922/60000373) at the Environmental Molecular Sciences Laboratory (EMSL), a national scientific user facility sponsored by the U.S. DOE's Office of Biological and Environmental Research and located at PNNL in Richland, WA. This research used the beamline 12-BM of the Advanced Photon Source, a U.S. Department of Energy (DOE) Office of Science user facility at Argonne National Laboratory and is based on research supported by the U.S. DOE Office of Science-Basic Energy Sciences, under Contract No. DE-AC02-06CH11357. Simulations were performed using PNNL Institutional Computing (PIC) and Mid-Range Scientific Computing resources. The authors thank PNNL scientist Charles T. Resch for help with the ICP-OES measurements.

REFERENCES

(1) Mudd, G. M.; Jowitt, S. M.; Werner, T. T. The world's lead-zinc mineral resources: scarcity, data, issues and opportunities. *Ore Geol. Rev.* **2017**, *80*, 1160-1190; DOI:10.1016/j.oregeorev.2016.08.010.

(2) Li, X.; Li, Z.; Lin, C.-J.; Bi, X.; Liu, J.; Feng, X.; Zhang, H.; Chen, J.; Wu, T. Health risks of heavy metal exposure through vegetable consumption near a large-scale Pb/Zn smelter in central China. *Ecotoxicol. Environ. Saf.* **2018**, *161*, 99-110; DOI:10.1016/j.ecoenv.2018.05.080.

(3) Casas, J. S.; Sordo, J. *Lead: chemistry, analytical aspects, environmental impact and health effects*; Elsevier, 2011.

(4) Liu, K.; Li, C.; Tang, S.; Shang, G.; Yu, F.; Li, Y. Heavy metal concentration, potential ecological risk assessment and enzyme activity in soils affected by a lead-zinc tailing spill in Guangxi, China. *Chemosphere* **2020**, *251*, 126415; DOI:10.1016/j.chemosphere.2020.126415.

(5) Goyer, R. A. Lead toxicity: current concerns. *Environ. Health Perspect.* **1993**, *100*, 177-187.
(6) Zhao, D.; Li, J.; Li, C.; Juhasz, A. L.; Scheckel, K. G.; Luo, J.; Li, H.-B.; Ma, L. Q. Lead relative bioavailability in lip products and their potential health risk to women. *Environ. Sci. Technol.* **2016**, *50* (11), 6036-6043; DOI:10.1021/acs.est.6b01425.
(7) Hashimoto, Y.; Takaoka, M.; Shiota, K. Enhanced transformation of lead speciation in rhizosphere soils using phosphorus amendments and phytostabilization: An X-ray absorption fine structure spectroscopy investigation. *J. Environ. Qual.* **2011**, *40* (3), 696-703; DOI:10.2134/jeq2010.0057.
(8) Hashimoto, Y.; Takaoka, M.; Oshita, K.; Tanida, H. Incomplete transformations of Pb to pyromorphite by phosphate-induced immobilization investigated by X-ray absorption fine structure (XAFS) spectroscopy. *Chemosphere* **2009**, *76* (5), 616-622; DOI:10.1016/j.chemosphere.2009.04.049.
(9) Lu, Y.; Hu, S.; Liang, Z.; Zhu, M.; Wang, Z.; Wang, X.; Liang, Y.; Dang, Z.; Shi, Z. Incorporation of Pb(II) into hematite during ferrihydrite transformation. *Environ. Sci. Nano* **2020**, *7* (3), 829-841; DOI:10.1039/C9EN01355E.
(10) O'Reilly, S. E.; Hochella Jr, M. F. Lead sorption efficiencies of natural and synthetic Mn and Fe-oxides. *Geochim. Cosmochim. Acta* **2003**, *67* (23), 4471-4487; DOI:10.1016/S0016-7037(03)00413-7.
(11) Dong, D.; Nelson, Y. M.; Lion, L. W.; Shuler, M. L.; Ghiorse, W. C. Adsorption of Pb and Cd onto metal oxides and organic material in natural surface coatings as determined by selective extractions: new evidence for the importance of Mn and Fe oxides. *Water Res.* **2000**, *34* (2), 427-436; DOI:10.1016/S0043-1354(99)00185-2.
(12) Michálková, Z.; Komárek, M.; Šillerová, H.; Della Puppa, L.; Joussein, E.; Bordas, F.; Vaněk, A.; Vaněk, O.; Ettler, V. Evaluating the potential of three Fe- and Mn-(nano) oxides for the stabilization of Cd, Cu and Pb in contaminated soils. *J. Environ. Manage.* **2014**, *146*, 226-234; DOI:10.1016/j.jenvman.2014.08.004.
(13) Li, Z.; Tang, L.; Zheng, Y.; Tian, D.; Su, M.; Zhang, F.; Ma, S.; Hu, S. Characterizing the mechanisms of lead immobilization via bioapatite and various clay minerals. *ACS Earth Space Chem.* **2017**, *1* (3), 152-157; DOI:10.1021/acsearthspacechem.7b00016.
(14) Yin, X.; Yu, L.; Luo, X.; Zhang, Z.; Sun, H.; Mosa, A. A.; Wang, N. Sorption of Pb(II) onto < 1 μm effective diameter clay minerals extracted from different soils of the Loess Plateau, China. *Geoderma* **2019**, *337*, 1058-1066; DOI:10.1016/j.geoderma.2018.11.027.
(15) Orucoglu, E.; Tournassat, C.; Robinet, J.-C.; Made, B.; Lundy, M. From experimental variability to the sorption related retention parameters necessary for performance assessment models for nuclear waste disposal systems: The example of Pb adsorption on clay minerals. *Appl. Clay Sci.* **2018**, *163*, 20-32; DOI:10.1016/j.clay.2018.07.003.
(16) Schmitt, D.; Taylor, H. E.; Aiken, G.; Roth, D.; Frimmel, F. Influence of natural organic matter on the adsorption of metal ions onto clay minerals. *Environ. Sci. Technol.* **2002**, *36* (13), 2932-2938; DOI:10.1021/es010271p.
(17) Guo, X.; Zhang, S.; Shan, X. q.; Luo, L.; Pei, Z.; Zhu, Y. G.; Liu, T.; Xie, Y. n.; Gault, A. Characterization of Pb, Cu, and Cd adsorption on particulate organic matter in soil. *Environ. Toxicol. Chem.* **2006**, *25* (9), 2366-2373; DOI:10.1897/05-636R.1.
(18) Lamelas, C.; Wilkinson, K. J.; Slaveykova, V. I. Influence of the composition of natural organic matter on Pb bioavailability to microalgae. *Environ. Sci. Technol.* **2005**, *39* (16), 6109-6116; DOI:10.1021/es050445t.
(19) Cornell, R. M.; Schwertmann, U. *The iron oxides: structure, properties, reactions, occurrences and uses*; John Wiley & Sons, 2003.
(20) Ponthieu, M.; Juillot, F.; Hiemstra, T.; Van Riemsdijk, W.; Benedetti, M. Metal ion binding to iron oxides. *Geochim. Cosmochim. Acta* **2006**, *70* (11), 2679-2698; DOI:10.1016/j.gca.2006.02.021.
(21) Hu, J. S.; Zhong, L. S.; Song, W. G.; Wan, L. J. Synthesis of hierarchically structured metal oxides and their application in heavy metal ion removal. Adv. Mater. 2008, 20 (15), 2977-2982; DOI:10.1002/adma.200800623.

(22) Liang, Y.; Wang, M.; Xiong, J.; Hou, J.; Wang, X.; Tan, W. Al-substitution-induced defect sites enhance adsorption of Pb^{2+} on hematite. *Environ. Sci. Nano* **2019**, *6* (5), 1323-1331; DOI:10.1039/C8EN01221K.
(23) Bargar, J.; Brown Jr, G.; Parks, G. Surface complexation of Pb (II) at oxide-water interfaces: II. XAFS and bond-valence determination of mononuclear Pb(II) sorption products and surface functional groups on iron oxides. *Geochim. Cosmochim. Acta* **1997**, *61* (13), 2639-2652; DOI:10.1016/S0016-7037(97)00124-5.
(24) Lenhart, J. J.; Bargar, J. R.; Davis, J. A. Spectroscopic evidence for ternary surface complexes in the lead(II)-malonic acid-hematite system. *J. Colloid Interface Sci.* **2001**, *234* (2), 448-452; DOI:10.1006/jcis.2000.7345.
(25) Huang, X.; Hou, X.; Zhang, X.; Rosso, K. M.; Zhang, L. Facet-dependent contaminant removal properties of hematite nanocrystals and their environmental implications. *Environ. Sci. Nano* **2018**, *5* (8), 1790-1806; DOI:10.1039/C8EN00548F.
(26) Wang, W.; Howe, J. Y.; Gu, B. Structure and morphology evolution of hematite (α-Fe_2O_3) nanoparticles in forced hydrolysis of ferric chloride. *J. Phys. Chem. C* **2008**, *112* (25), 9203-9208; DOI:10.1021/jp800683j.
(27) Bargar, J. R.; Trainor, T. P.; Fitts, J. P.; Chambers, S. A.; Brown, G. E. In situ grazing-incidence extended X-ray absorption fine structure study of Pb(II) chemisorption on hematite (0001) and (1-102) surfaces. *Langmuir* **2004**, *20* (5), 1667-1673; DOI:10.1021/la0354133.
(28) Mason, S. E.; Iceman, C. R.; Tanwar, K. S.; Trainor, T. P.; Chaka, A. M. Pb(II) adsorption on isostructural hydrated alumina and hematite (0001) surfaces: A DFT study. *J. Phys. Chem. C* **2009**, *113* (6), 2159-2170; DOI:10.1021/jp807321e.
(29) Noerpel, M. R.; Lee, S. S.; Lenhart, J. J. X-ray analyses of lead adsorption on the (001), (110), and (012) hematite surfaces. *Environ. Sci. Technol.* **2016**, *50* (22), 12283-12291; DOI:10.1021/acs.est.6b03913.
(30) Qiu, C.; Majs, F.; Eng, P. J.; Stubbs, J. E.; Douglas, T. A.; Schmidt, M.; Trainor, T. P. In situ structural study of the surface complexation of lead(II) on the chemically mechanically polished hematite (1-102) surface. *J. Colloid Interface Sci.* **2018**, *524*, 65-75; DOI:10.1016/j.jcis.2018.04.005.
(31) Qiu, C.; Chen, W.; Schmidt, M.; Majs, F.; Douglas, T. A.; Trainor, T. P. Selective adsorption of Pb(II) on an annealed hematite (1-102) surface: Evidence from crystal truncation rod X-ray diffraction and density functional theory. *Environ. Sci. Technol.* **2020**, *54* (11), 6651-6660; DOI:10.1021/acs.est.0c00060.
(32) Liang, Y.; Xiang, Y.; Wei, Z.; Avena, M.; Xiong, J.; Hou, J.; Wang, M.; Tan, W. Complexation mechanism of Pb^{2+} on Al-substituted hematite: A modeling study and theoretical calculation. *Environ. Res.* **2024**, *252*, 118935; DOI:10.1016/j.envres.2024.118935.
(33) Liang, Y.; Xu, J.; Koopal, L. K.; Wang, M.; Xiong, J.; Hou, J.; Tan, W. Facet-dependent surface charge and Pb^{2+} adsorption characteristics of hematite nanoparticles: CD-MUSIC-eSGC modeling. *Environ. Res.* **2021**, *196*, 110383; DOI:10.1016/j.envres.2020.110383.
(34) Xiang, Y.; Liu, J.; Chen, Y.; Zhang, H.; Ren, L.; Ye, B.; Tan, W.; Andreas, K.; Hou, J. The change of coordination environments induced by vacancy defects in hematite leads to a contrasting difference between cation Pb(II) and oxyanion As(V) immobilization. *Environ. Pollut.* **2024**, *344*, 123318; DOI:10.1016/j.envpol.2024.123318.
(35) Mei, H.; Liu, Y.; Tan, X.; Feng, J.; Ai, Y.; Fang, M. U(VI) adsorption on hematite nanocrystals: Insights into the reactivity of {001} and {012} facets. *J. Hazard. Mater.* **2020**, *399*, 123028; DOI:10.1016/j.jhazmat.2020.123028.
(36) Chen, W.; Guo, G.; Huang, L.; Ouyang, L.; Shuai, Q. Facet-dependent adsorption of aromatic organoarsenicals on hematite: The mechanism and environmental impact. *J. Hazard. Mater.* **2024**, *464*, 132976; DOI:10.1016/j.jhazmat.2023.132976.
(37) Zong, M. R.; Zhang, X.; Wang, Y. N.; Huang, X. P.; Zhou, J. B.; Wang, Z. M.; De Yoreo, J. J.; Lu, X. C.; Rosso, K. M. Synthesis of 2D hexagonal hematite nanosheets and the crystal growth mechanism. *Inorg. Chem.* **2019**, *58* (24), 16727-16735; DOI:10.1021/acs.inorgchem.9b02883.

(38) Chatman, S.; Zarzycki, P.; Rosso, K. M. Surface potentials of (001), (012), (113) hematite (α-Fe_2O_3) crystal faces in aqueous solution. *Phys. Chem. Chem. Phys.* **2013**, *15* (33), 13911-13921; DOI:10.1039/C3CP52592A.
(39) Chan, J.; Ang, S.; Ye, E.; Sullivan, M.; Zhang, J.; Lin, M. Heterogeneous photo-Fenton reaction on hematite (α-Fe_2O_3) {104}, {113} and {001} surface facets. *Phys. Chem. Chem. Phys.* **2015**, *17* (38), 25333-25341; DOI:10.1039/C5CP03332B.
(40) Zong, M.; Song, D.; Zhang, X.; Huang, X.; Lu, X.; Rosso, K. M. Facet-dependent photodegradation of methylene blue by hematite nanoplates in visible light. *Environ. Sci. Technol.* **2020**, *55* (1), 677-688; DOI:10.1021/acs.est.0c05592.
(41) Zhang, H.; Xu, Z.; Chen, D.; Hu, B.; Zhou, Q.; Chen, S.; Li, S.; Sun, W.; Zhang, C. Adsorption mechanism of water molecules on hematite (104) surface and the hydration microstructure. *Appl. Surf. Sci.* **2021**, *550*, 149328; DOI:10.1016/j.apsusc.2021.149328.
(42) Huang, X.; Hou, X.; Wang, F.; Guo, B.; Song, F.; Ling, L.; Zhao, J.; Zhang, L. Molecular-scale structures of uranyl surface complexes on hematite facets. *Environ. Sci. Nano* **2019**, *6* (3), 892-903; DOI:10.1039/C8EN00899J.
(43) Podsiadły-Paszkowska, A.; Tranca, I.; Szyja, B. M. Tuning the hematite (110) surface properties to enhance its efficiency in photoelectrochemistry. *J. Phys. Chem. C* **2019**, *123* (9), 5401-5410; DOI:10.1021/acs.jpcc.8b10872.
(44) Zhou, J.; Song, D.; Mergelsberg, S. T.; Wang, Y.; Adhikari, N. M.; Lahiri, N.; Zhao, Y.; Chen, P.; Wang, Z.; Zhang, X. Facet-dependent dispersion and aggregation of aqueous hematite nanoparticles. *Sci. Adv.* **2024**, *10* (7), eadi7494; DOI:10.1126/sciadv.adi7494.
(45) Wang, Y.; Xue, S.; Lin, Q.; Song, D.; He, Y.; Liu, L.; Zhou, J.; Zong, M.; De Yoreo, J. J.; Zhu, J. Particle-based hematite crystallization is invariant to initial particle morphology. *Proc. Natl. Acad. Sci. U. S. A.* **2022**, *119* (11), e2112679119; DOI:10.1073/pnas.2112679119.
(46) Hao, T.; Huang, Y.; Li, F.; Wu, Y.; Fang, L. Facet-dependent Fe(II) redox chemistry on iron oxide for organic pollutant transformation and mechanisms. *Water Res.* **2022**, *219*, 118587; DOI:10.1016/j.watres.2022.118587.
(47) Guo, H.; Barnard, A. S. Naturally occurring iron oxide nanoparticles: morphology, surface chemistry and environmental stability. *J. Mater. Chem. A* **2013**, *1* (1), 27-42; DOI:10.1039/C2TA00523A.
(48) Wang, W.; Yang, L.; Gao, D.; Yu, M.; Jiang, S.; Li, J.; Zhang, J.; Feng, X.; Tan, W.; Liu, F. Characteristics of iron (hydr) oxides and Cr(VI) retention mechanisms in soils from tropical and subtropical areas of China. *J. Hazard. Mater.* **2024**, *465*, 133107; DOI:10.1016/j.jhazmat.2023.133107.
(49) Guo, H.; Xu, H.; Barnard, A. S. Can hematite nanoparticles be an environmental indicator? *Energy Environ. Sci.* **2013**, *6* (2), 561-569; DOI:10.1039/C2EE23253G.
(50) Melchor-Martínez, E. M.; Macias-Garbett, R.; Malacara-Becerra, A.; Iqbal, H. M.; Sosa-Hernández, J. E.; Parra-Saldívar, R. Environmental impact of emerging contaminants from battery waste: A mini review. *Case Stud. Chem. Environ. Eng.* **2021**, *3*, 100104; DOI:10.1016/j.cscee.2021.100104.
(51) Rajoria, S.; Vashishtha, M.; Sangal, V. K. Treatment of electroplating industry wastewater: a review on the various techniques. *Environ. Sci. Pollut. Res.* **2022**, *29* (48), 72196-72246; DOI:10.1007/s11356-022-18643-y.
(52) Wu, P.; Jiang, L. Y.; He, Z.; Song, Y. Treatment of metallurgical industry wastewater for organic contaminant removal in China: status, challenges, and perspectives. *Environ. Sci.: Water Res. Technol.* **2017**, *3* (6), 1015-1031; DOI:10.1039/C7EW00097A.
(53) Iakovleva, E.; Sillanpää, M. The use of low-cost adsorbents for wastewater purification in mining industries. *Environ. Sci. Pollut. Res.* **2013**, *20*, 7878-7899; DOI:10.1007/s11356-013-1546-8.
(54) Ravel, B.; Newville, M. ATHENA, ARTEMIS, HEPHAESTUS: data analysis for X-ray absorption spectroscopy using IFEFFIT. *J. Synchrotron Radiat.* **2005**, *12* (4), 537-541; DOI:10.1107/S0909049505012719.
(55) Newville, M. Larch: An Analysis Package for XAFS and Related Spectroscopies. *J. Phys.: Conf. Ser.* **2013**, *430*, 012007; DOI:10.1088/1742-6596/430/1/012007.

(56) Rehr, J. J.; Kas, J. J.; Prange, M. P.; Sorini, A. P.; Takimoto, Y.; Vila, F. Ab initio theory and calculations of X-ray spectra. *C. R. Phys.* **2009**, *10* (6), 548-559; DOI:10.1016/j.crhy.2008.08.004.
(57) Calvin, S. *XAFS for Everyone*; CRC Press, 2013.
(58) Valiev, M.; Bylaska, E. J.; Govind, N.; Kowalski, K.; Straatsma, T. P.; Van Dam, H. J. J.; Wang, D.; Nieplocha, J.; Aprà, E.; Windus, T. L. NWChem: A comprehensive and scalable open-source solution for large scale molecular simulations. *Comput. Phys. Commun.* **2010**, *181* (9), 1477-1489; DOI:10.1016/j.cpc.2010.04.018.
(59) Apra, E.; Bylaska, E. J.; De Jong, W. A.; Govind, N.; Kowalski, K.; Straatsma, T. P.; Valiev, M.; van Dam, H. J.; Alexeev, Y.; Anchell, J. NWChem: Past, present, and future. *J. Chem. Phys.* **2020**, *152* (18), 184102; DOI:10.1063/5.0004997.
(60) Perdew, J. P.; Burke, K.; Ernzerhof, M. Generalized gradient approximation made simple. *Phys. Rev. Lett.* **1996**, *77* (18), 3865; DOI:10.1103/PhysRevLett.77.3865.
(61) Dudarev, S. L.; Botton, G. A.; Savrasov, S. Y.; Humphreys, C. J.; Sutton, A. P. Electron-energy-loss spectra and the structural stability of nickel oxide: An LSDA+U study. *Phys. Rev. B* **1998**, *57* (3), 1505-1509; DOI:10.1103/PhysRevB.57.1505.
(62) Chen, P.; Song, D.; Zhang, X.; Xie, Q.; Zhou, Y.; Liu, H.; Xu, L.; Chen, T.; Rosso, K. M. Understanding competitive phosphate and silicate adsorption on goethite by connecting batch experiments with density functional theory calculations. *Environ. Sci. Technol.* **2022**, *56* (2), 823-834; DOI:10.1021/acs.est.1c03629.
(63) Kleinman, L.; Bylander, D. Efficacious form for model pseudopotentials. *Phys. Rev. Lett.* **1982**, *48* (20), 1425; DOI:10.1103/PhysRevLett.48.1425.
(64) Bylaska, E. J.; Song, D.; Rosso, K. M. Electron transfer calculations between edge sharing octahedra in hematite, goethite, and annite. *Geochim. Cosmochim. Acta* **2020**, *291*, 79-91; DOI:10.1016/j.gca.2020.04.036.
(65) Grimme, S.; Ehrlich, S.; Goerigk, L. Effect of the Damping Function in Dispersion Corrected Density Functional Theory. *J. Comput. Chem.* **2011**, *32* (7), 1456-1465; DOI:10.1002/jcc.21759.
(66) Demangeat, E.; Pédrot, M.; Dia, A.; Bouhnik-le-Coz, M.; Grasset, F.; Hanna, K.; Kamagate, M.; Cabello-Hurtado, F. Colloidal and chemical stabilities of iron oxide nanoparticles in aqueous solutions: the interplay of structural, chemical and environmental drivers. *Environ. Sci. Nano* **2018**, *5* (4), 992-1001; DOI:10.1039/C7EN01159H.
(67) Lanzl, C. A.; Baltrusaitis, J.; Cwiertny, D. M. Dissolution of hematite nanoparticle aggregates: influence of primary particle size, dissolution mechanism, and solution pH. *Langmuir* **2012**, *28* (45), 15797-15808; DOI: 10.1021/la3022497.
(68) Simonin, J.-P. On the comparison of pseudo-first order and pseudo-second order rate laws in the modeling of adsorption kinetics. *Chem. Eng. J.* **2016**, *300*, 254-263; DOI:10.1016/j.cej.2016.04.079.
(69) Li, M.; Liu, H.; Chen, T.; Chen, D.; Wang, C.; Wei, L.; Wang, L. Efficient U(VI) adsorption on iron/carbon composites derived from the coupling of cellulose with iron oxides: Performance and mechanism. *Sci. Total Environ.* **2020**, *703*, 135604; DOI:10.1016/j.scitotenv.2019.135604.
(70) Chen, P.; Zhou, Y.; Xie, Q.; Chen, T.; Liu, H.; Xue, S.; Zou, X.; Wei, L.; Xu, L.; Zhang, X. Phosphate adsorption kinetics and equilibria on natural iron and manganese oxide composites. *J. Environ. Manage.* **2022**, *323*, 116222; DOI:10.1016/j.jenvman.2022.116222.
(71) Sreejalekshmi, K.; Krishnan, K. A.; Anirudhan, T. Adsorption of Pb(II) and Pb(II)-citric acid on sawdust activated carbon: Kinetic and equilibrium isotherm studies. *J. Hazard. Mater.* **2009**, *161* (2-3), 1506-1513; DOI:10.1016/j.jhazmat.2008.05.002.
(72) Li, M.; Liu, H.; Chen, T.; Dong, C.; Sun, Y. Synthesis of magnetic biochar composites for enhanced uranium(VI) adsorption. *Sci. Total Environ.* **2019**, *651*, 1020-1028; DOI:10.1016/j.scitotenv.2018.09.259.
(73) Gouda, M. Synthesis and characterization of hematite nanoparticles for removal of Pb^{2+} and Cu^{2+} from water samples. *Nucl. Sci. Sci. J.* **2024**, *13* (1), 100-109; DOI:10.21608/nssj.2024.216205.1010.
(74) Zhao, D.; Chen, C.; Sheng, G.; Wang, X. Effect of environmental conditions on the retention behaviour of Pb(II) by hematite. *J. Chem. Technol. Biotechnol.* **2011**, *86* (8), 1099-1106; DOI:10.1002/jctb.2623.

(75) Bailliez, S.; Nzihou, A.; Beche, E.; Flamant, G. Removal of lead (Pb) by hydroxyapatite sorbent. *Process Saf. Environ. Prot.* **2004**, *82* (2), 175-180; DOI:10.1205/095758204322972816.
(76) Jiang, M. Q.; Wang, Q. P.; Jin, X. Y.; Chen, Z. L. Removal of Pb(II) from aqueous solution using modified and unmodified kaolinite clay. *J. Hazard. Mater.* **2009**, *170* (1), 332-339; DOI:10.1016/j.jhazmat.2009.04.092.
(77) Fan, Q.; Li, Z.; Zhao, H.; Jia, Z.; Xu, J.; Wu, W. Adsorption of Pb(II) on palygorskite from aqueous solution: effects of pH, ionic strength and temperature. *Appl. Clay Sci.* **2009**, *45* (3), 111-116; DOI:10.1016/j.clay.2009.04.009.
(78) Liu, H.; Lu, X.; Li, M.; Zhang, L.; Pan, C.; Zhang, R.; Li, J.; Xiang, W. Structural incorporation of manganese into goethite and its enhancement of Pb(II) adsorption. *Environ. Sci. Technol.* **2018**, *52* (8), 4719-4727; DOI:10.1021/acs.est.7b05612.
(79) Al-Degs, Y.; Khraisheh, M.; Tutunji, M. Sorption of lead ions on diatomite and manganese oxides modified diatomite. *Water Res.* **2001**, *35* (15), 3724-3728; DOI:10.1016/S0043-1354(01)00071-9.
(80) Yavuz, Ö.; Guzel, R.; Aydin, F.; Tegin, I.; Ziyadanogullari, R. Removal of Cadmium and Lead from Aqueous Solution by Calcite. *Pol. J. Environ. Stud.* **2007**, *16* (3), 467-471.
(81) Zhang, S. Q.; Hou, W. G. Adsorption behavior of Pb(II) on montmorillonite. *Colloids Surf. Physicochem. Eng. Aspects* **2008**, *320* (1-3), 92-97; DOI:10.1016/j.colsurfa.2008.01.038.
(82) Zhao, D.; Yang, X.; Zhang, H.; Chen, C.; Wang, X. Effect of environmental conditions on Pb(II) adsorption on β-MnO_2. *Chem. Eng. J.* **2010**, *164* (1), 49-55; DOI:10.1016/j.cej.2010.08.014.
(83) Mao, M.; Yan, T.; Chen, G.; Zhang, J.; Shi, L.; Zhang, D. Selective capacitive removal of Pb^{2+} from wastewater over redox-active electrodes. *Environ. Sci. Technol.* **2020**, *55* (1), 730-737; DOI:10.1021/acs.est.0c06562.
(84) Baltrusaitis, J.; Chen, H.; Rubasinghege, G.; Grassian, V. H. Heterogeneous atmospheric chemistry of lead oxide particles with nitrogen dioxide increases lead solubility: environmental and health implications. *Environ. Sci. Technol.* **2012**, *46* (23), 12806-12813; DOI:10.1021/es3019572.
(85) Lu, B.; Liu, Q.; Chen, S. Electrocatalysis of single-atom sites: impacts of atomic coordination. *ACS Catal.* **2020**, *10* (14), 7584-7618; DOI:10.1021/acscatal.0c01950.
(86) Bargar, J.; Brown Jr, G.; Parks, G. Surface complexation of Pb(II) at oxide-water interfaces: III. XAFS determination of Pb(II) and Pb(II)-chloro adsorption complexes on goethite and alumina. *Geochim. Cosmochim. Acta* **1998**, *62* (2), 193-207; DOI:10.1016/S0016-7037(97)00334-7.
(87) Barrón, V.; Torrent, J. Surface hydroxyl configuration of various crystal faces of hematite and goethite. *J. Colloid Interface Sci.* **1996**, *177* (2), 407-410; DOI:10.1006/jcis.1996.0051.
(88) Wang, L.; Zhou, J. C.; Li, Z. H.; Zhang, X.; Leung, K. M. Y.; Yuan, L.; Sheng, G. P. Facet-specific photocatalytic degradation of extracellular antibiotic resistance genes by hematite nanoparticles in aquatic environments. *Environ. Sci. Technol.* **2023**, *57* (51), 21835-21845; DOI:10.1021/acs.est.3c06571.
(89) Lv, J.; Miao, Y.; Huang, Z.; Han, R.; Zhang, S. Facet-mediated adsorption and molecular fractionation of humic substances on hematite surfaces. *Environ. Sci. Technol.* **2018**, *52* (20), 11660-11669; DOI:10.1021/acs.est.8b03940.
(90) He, J.; Xiong, D.; Zhou, P.; Xiao, X.; Ni, F.; Deng, S.; Shen, F.; Tian, D.; Long, L.; Luo, L. A novel homogenous in-situ generated ferrihydrite nanoparticles/polyethersulfone composite membrane for removal of lead from water: Development, characterization, performance and mechanism. *Chem. Eng. J.* **2020**, *393*, 124696; DOI:10.1016/j.cej.2020.124696.
(91) Peacock, C. L.; Sherman, D. M. Copper(II) sorption onto goethite, hematite and lepidocrocite: a surface complexation model based on ab initio molecular geometries and EXAFS spectroscopy. *Geochim. Cosmochim. Acta* **2004**, *68* (12), 2623-2637; DOI:10.1016/j.gca.2003.11.030.
(92) Ha, J.; Trainor, T. P.; Farges, F.; Brown Jr, G. E. Interaction of aqueous Zn(II) with hematite nanoparticles and microparticles. Part 1. EXAFS study of Zn(II) adsorption and precipitation. *Langmuir* **2009**, *25* (10), 5574-5585; DOI:10.1021/la8028947.

803 **TOC**

804 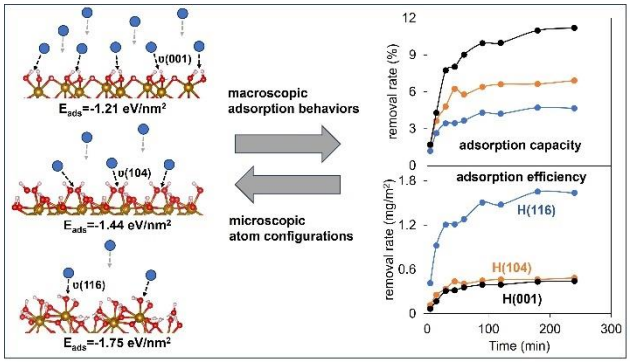

805